



# Validating MRI-Derived Myocardial Stiffness Estimates Using *In Vitro* Synthetic Heart Models

Fikunwa O. Kolawole<sup>1,2,3</sup> · Mathias Peirlinck<sup>4</sup> · Tyler E. Cork<sup>1,2,5</sup> · Marc Levenston<sup>1,3</sup> · Ellen Kuhl<sup>3</sup> · Daniel B. Ennis<sup>1,2</sup>

Received: 19 September 2022 / Accepted: 7 February 2023 / Published online: 13 March 2023  
© The Author(s) under exclusive licence to Biomedical Engineering Society 2023

## Abstract

Impaired cardiac filling in response to increased passive myocardial stiffness contributes to the pathophysiology of heart failure. By leveraging cardiac MRI data and ventricular pressure measurements, we can estimate *in vivo* passive myocardial stiffness using personalized inverse finite element models. While it is well-known that this approach is subject to uncertainties, only few studies quantify the accuracy of these stiffness estimates. This lack of validation is, at least in part, due to the absence of ground truth *in vivo* passive myocardial stiffness values. Here, using 3D printing, we created soft, homogenous, isotropic, hyperelastic heart phantoms of varying geometry and stiffness and simulate diastolic filling by incorporating the phantoms into an MRI-compatible left ventricular inflation system. We estimate phantom stiffness from MRI and pressure data using inverse finite element analyses based on a Neo-Hookean model. We demonstrate that our identified softest and stiffest values of 215.7 and 512.3 kPa agree well with the ground truth of 226.2 and 526.4 kPa. Overall, our estimated stiffnesses revealed a good agreement with the ground truth (< 5.8% error) across all models. Our results suggest that MRI-driven computational constitutive modeling can accurately estimate synthetic heart material stiffnesses in the range of 200–500 kPa.

**Keywords** Cardiac mechanics · Cardiac MRI · Heart failure · 3D printed phantom · *In vitro* MRI · Passive myocardial stiffness · Hyperelastic materials

## Introduction

Impaired cardiac filling contributes to the pathophysiology of many cardiac diseases<sup>22</sup> which can eventually degenerate into heart failure. This multifaceted clinical syndrome is characterized by the heart's inability to supply adequate blood to meet the metabolic demands of the body.<sup>8</sup> Heart

failure is a global public health issue with significant mortality and morbidity<sup>29</sup> and high socioeconomic burden.<sup>46</sup> The high prevalence of heart failure<sup>52</sup> is also projected to continue increasing over the next decade.<sup>27</sup>

Diastolic dysfunction, which could be due to abnormal active relaxation<sup>51</sup> and/or diastolic chamber stiffness,<sup>62</sup> is observed in nearly half of heart failure patients, who are said to have heart failure with preserved (i.e. relatively normal) ejection fraction (HFpEF).<sup>64</sup> In these patients, though

Associate Editor Jane Grande-Allen oversaw the review of this article.

✉ Fikunwa O. Kolawole  
fikunwa@stanford.edu

Mathias Peirlinck  
mplab-3me@tudelft.nl

Tyler E. Cork  
tecork@stanford.edu

Marc Levenston  
levenston@stanford.edu

Ellen Kuhl  
ekuhl@stanford.edu

Daniel B. Ennis  
dbe@stanford.edu

<sup>1</sup> Department of Radiology, Stanford University, Stanford, CA 94305, USA

<sup>2</sup> Division of Radiology, Veterans Administration Health Care System, Palo Alto, CA 94304, USA

<sup>3</sup> Department of Mechanical Engineering, Stanford University, Stanford, CA 94305, USA

<sup>4</sup> Department of Biomechanical Engineering, Delft University of Technology, Delft, Netherlands

<sup>5</sup> Department of Bioengineering, Stanford University, Stanford, CA 94305, USA

ejection fraction is maintained, multiscale remodeling leads to impaired LV diastolic filling resulting in inadequate cardiac output. Passive stiffness of myocardium, the cardiac muscle tissue, regulates diastolic filling<sup>62</sup> and increased passive myocardial stiffness is a significant remodeling mechanism implicated in the etiology of HFpEF.<sup>44</sup> To improve understanding and management of HFpEF, a clinical method to reliably identify changes in passive myocardial stiffness is a necessity.<sup>16</sup> Moreover, other diseases where passive myocardial stiffness is altered due to pathophysiological remodeling of the cardiomyocytes and extracellular matrix (e.g. hypertrophic cardiomyopathy) can benefit from a method for clinical estimation of passive myocardial stiffness.

Medical imaging-based computational constitutive modeling enables estimation of patient-specific *in vivo* passive myocardial stiffness,<sup>38,56</sup> a biomechanical metric with significant prognostic value for HFpEF patients.<sup>58</sup> Cardiac MRI sequences can be used to acquire data needed for computational modeling: high resolution cardiac geometry, cardiac motion and local displacements, and boundary conditions. While subject-specific cardiac microstructural organization can be obtained using *in vivo* cDTI,<sup>1,49</sup> the method is still limited by issues such as low spatial resolution and signal-to-noise ratio. Ventricular pressures, which are also necessary for computational modeling can be acquired invasively through catheterization or estimated non-invasively through Doppler echocardiography.<sup>6,13</sup>

Numerous studies combine cardiac MRI, ventricular pressures, and inverse finite element modeling to estimate *in vivo* passive myocardial mechanical behavior and stiffness in computational models.<sup>3,14,18,24,31,37,40,42,53,55,57,59,60</sup> Through these patient-specific simulations, certain metrics of cardiac function that are otherwise difficult to measure directly, such as wall stresses and strains, can be estimated. This personalized understanding of cardiac function can reveal disease mechanisms that can be therapeutic targets.<sup>45</sup> However, before these techniques for estimating *in vivo* passive myocardial stiffness can be adopted clinically, they need to be thoroughly validated.

Although the patient-specific data needed to estimate *in vivo* passive myocardial stiffness are unavoidably subject to uncertainty,<sup>25,41,43,50</sup> we lack detailed studies evaluating the accuracy and precision of MRI-based *in vivo* passive myocardial stiffness estimation. Moreover, the data acquisition and analysis techniques employed for MRI-driven stiffness estimation can vary significantly due to lack of a consensus. There is, however, a dearth of studies on the accuracy and precision of these MRI-based myocardial stiffness estimation methods. This lack of validation is largely because of the absence of ground truth *in vivo* passive stiffness estimates. Overcoming this validation gridlock necessitates the development of a highly controlled *in vitro* stiffness

estimation framework that incorporates heart phantoms of known stiffness properties.

We addressed this unique validation challenge by developing soft, MRI-visible heart phantoms of known stiffness. The phantoms were incorporated within an *in vitro* MRI-compatible flow loop to fill the phantom's LV, simulating cardiac diastolic filling. Using MRI-driven computational modeling, the acquired MRI and ventricular pressure data of the phantom during inflation was used to estimate the material stiffness of the phantom's ventricular wall. To quantify the accuracy of our method, the estimated stiffness was then compared to ground truth measures of the phantom material stiffness obtained through tensile testing. We used heart phantoms of varying stiffness to quantify our ability to identify stiffness changes. Phantoms of different geometries were also used to assess the identifiability of stiffness independent of geometry. In this work, we validate a material stiffness estimation framework in soft, homogenous, isotropic hyperelastic heart-like phantoms of varying stiffness and geometrical complexity. In doing so, we demonstrate the feasibility and intrinsic challenges of using MRI-driven computational constitutive modeling for accurate identification of material stiffness in heart-like phantoms that resemble *in vivo* passive myocardial stiffness.

## Materials and Methods

We describe the heart phantom development (“[Phantom Development](#)” section), the ground truth characterization of the phantom material's mechanical properties (“[Ground Truth Material Characterization](#)” section), the *in vitro* ventricular filling setup, acquisition of the heart phantom's unloaded geometry, filling volumes and pressures (“[Imaging Experiments](#)” section), the data analysis strategy (“[Data Analysis](#)” section), and lastly, the *in silico* calibration of material parameters using the experimentally derived LV pressure–volume relation (“[In Silico Modeling and Stiffness Quantification](#)” section).

### Phantom Development

Our study used four different heart phantoms. Three of these had the same geometry ( $g_i$ ), but different material stiffness ( $s_j$ ) (referred to as  $M_{g1,s1}$   $M_{g1,s2}$   $M_{g1,s3}$ ), with model  $M_{g1,s1}$  being the softest and model  $M_{g1,s3}$  being the stiffest. To understand the possible effects of geometry on the accuracy of the stiffness estimates, the final model ( $M_{g2,s1}$ ) was manufactured with material of a similar stiffness to model  $M_{g1,s1}$ , but with a different geometry.

We generated 3D geometric heart models by segmenting (MITK v2018.04.2) high-resolution T1-weighted images from healthy *ex vivo* porcine subjects (restored to *in vivo*

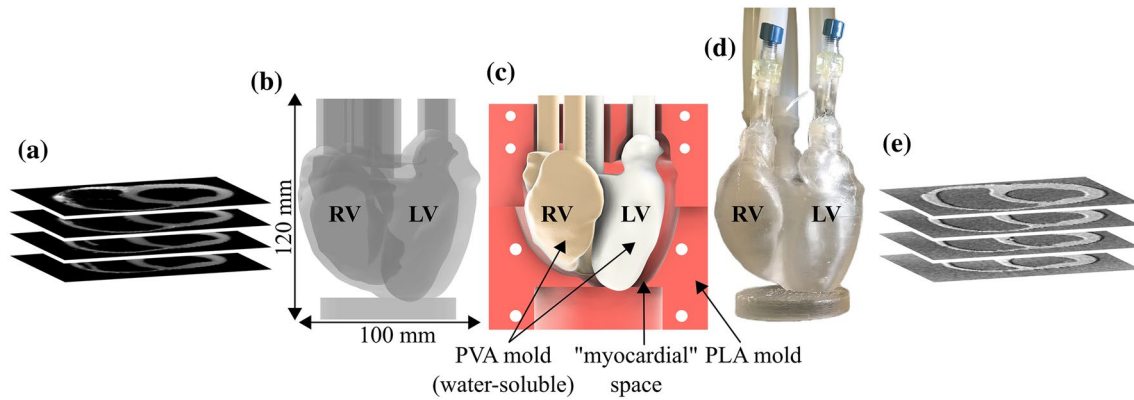


**Figure 1** Phantom manufacturing process: (a) *ex vivo* porcine T1-weighted images (at mid-diastasis) were segmented to develop the geometric heart model. (b) The model was fitted with basal ports for volume loading and an apical anchor was added to fix the apex during experiments. (c) The phantom was manufactured by curing a silicone elastomer blend in a 3D printed PLA/PVA mold for 48 h. The LV and

RV blood pool casts were printed with water-soluble PVA. (d) The subject-specific phantom was fitted with 3D printed barbed connectors and tubing for loading and pressure measurements. (e) Unloaded 3D SPGR images of the 3D printed phantom shows high geometric agreement with porcine subject images.

mid-diastasis geometry)<sup>7</sup> (Fig. 1a). The geometric models were designed to include basal ventricular ports and an apical anchor to facilitate loading and motion stabilization (Fusion 360, Autodesk) (Fig. 1b) The heart phantoms were designed to primarily be composed of the LV and RV, but some extent of the atrial myocardium was included to ease the addition of the basal ports needed for volume control and loading.

The heart phantoms were manufactured to match, as closely as feasible, both the mechanical and MRI relaxation properties of human ventricular myocardium. Direct 3D printing of suitably soft materials is currently infeasible; therefore, the heart phantoms were cast using a combination of epicardial and endocardial molds. To develop the phantoms, we employed a lost-wax casting technique that has been used to manufacture anatomically detailed heart phantoms.<sup>9</sup>

A negative epicardial mold was created using the epicardial surface of the 3D geometric heart models. The ventricular blood pool segmentations were used to create left ventricle (LV) and right ventricle (RV) blood pool casts (endocardial molds). The epicardial and endocardial molds were converted into stereolithography files and 3D printed (Ultimaker 3 Extended) using tough polylactic acid and water-soluble polyvinyl alcohol, respectively. The “myocardial” space between the nested molds was then injected with a blend of silicone elastomers (Sylgard 184 and 527, Dow Corning). The models were then left to cure in the 3D printed mold for 48 hours at room temperature (Fig. 1c), after which the mold parts were removed and the blood pool casts were dissolved in water. Finally, the heart phantoms were fitted with adapter parts (Fig. 2b) at the basal ventricular ports for attachment of tubing to connect the phantoms to the flow loop.

Using this technique, we produced subject-specific heart phantoms of high geometric fidelity and both passive stiffness and MRI relaxation properties<sup>23</sup> that approximate ventricular myocardium. The stiffness of Sylgard blends can be tuned by varying the mass composition of its constituents,<sup>36</sup> therefore we were also able to produce heart phantoms with a range of stiffness. Three silicone elastomer blends containing a mass ratio of Sylgard 184 to Sylgard 527 of 20:80, 25:75, and 30:70 respectively, were used to produce phantom materials with increasing stiffness.

### Ground Truth Material Characterization

The ground truth stiffness of the silicone elastomer blends used to manufacture the phantoms were assessed via uniaxial tensile testing. Testing samples were produced in parallel with the phantom development and were subjected to identical curing conditions as the associated heart phantoms. Samples of uniform width (12 mm) were cut out from cured sheets of uniform thickness (3 mm) and were subsequently mechanically tested according to a modified ASTM D412 standard using a material testing machine (Instron 5848 Microtester, 100 N load cell). The samples were mounted by first clamping the specimen to the upper grip, zeroing the load cell, then clamping the specimen to the lower grip while taking care to avoid load application. The grip-to-grip lengths of the mounted samples were used as the gauge lengths since the samples were attached such that the width and thickness in the grip-to-grip region was uniform. We did not directly measure the strains in the samples because clamping an extensometer onto these soft samples was found to appreciably affect the forces measured. Instead, to calculate the principal stretch in each sample, the extension from

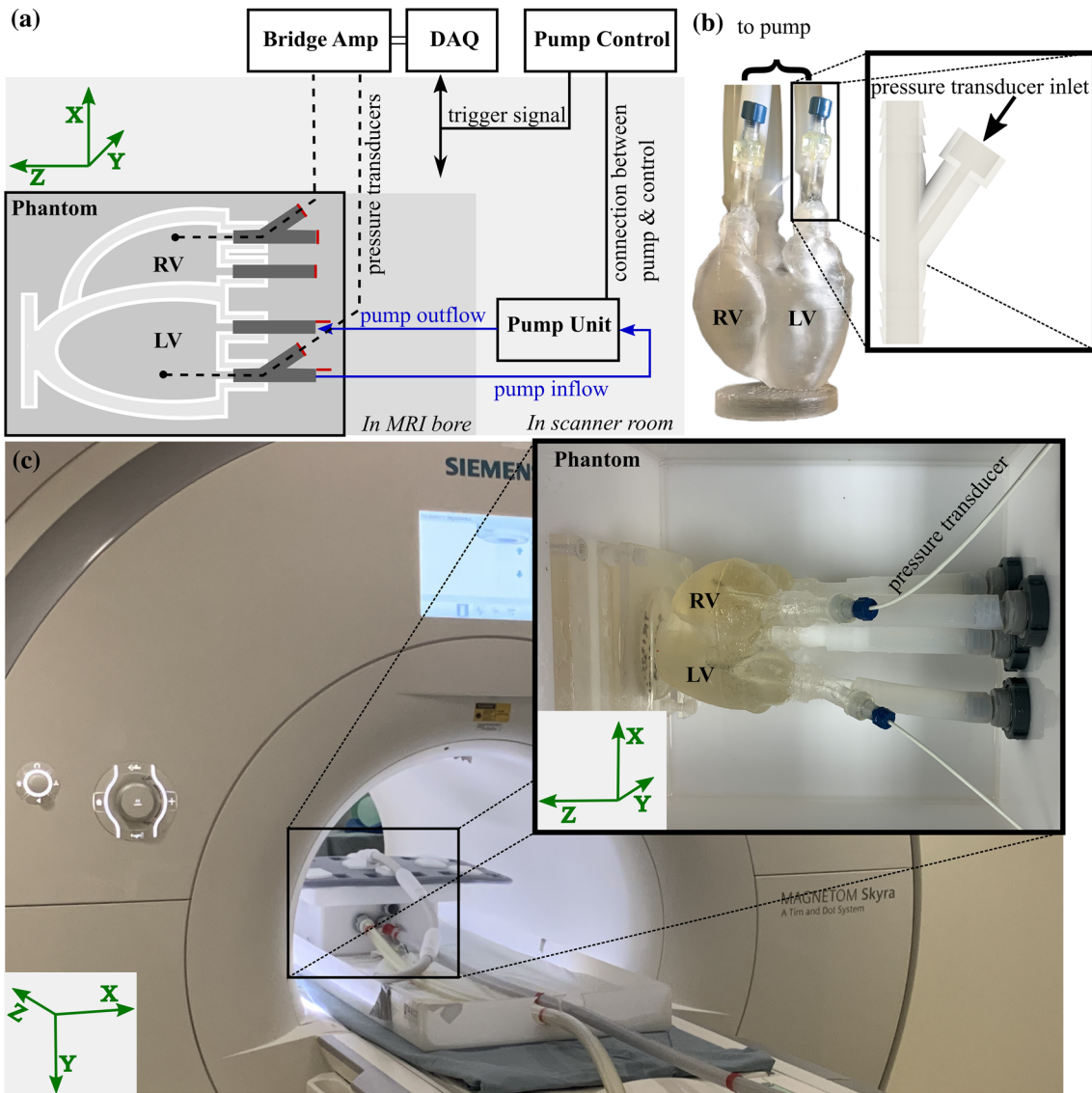


**Figure 2** Experimental setup schematic. (a) The heart phantom is connected to an MRI-compatible flow loop and fixed at the apex and basal ports. The programmable flow pump is used to inflate the phantom’s left ventricle (LV), while the right ventricle (RV) is kept at constant volume. Pressure transducers were used to record the intraven-

tricular filling pressures simultaneously. (b) The heart phantom was adapted with tubing for connection to the flow loop. The custom-built barbed adapter with inlets for the pressure transducer is highlighted. (c) Phantom inflation setup inside scanner. Inside of the phantom box is highlighted.

the tensile tester was used with the gauge length, which was set to 65 mm.

We considered the potential effects of viscoelasticity in our samples by assessing the effects of strain rates on the mechanical behavior and didn’t find significant strain rate effects which is consistent with previous work in literature that assessed strain rate effects on the mechanical behavior of Sylgard.<sup>17,20</sup> Hence, we modeled the phantom materials as effectively hyperelastic. The test was performed at ambient conditions with a strain rate of 10%/s which was the closest we could get to the maximum strain rate in the *in vitro* phantoms.

For each model, three separate samples were tested, and the averaged stress–stretch data across all three samples was used as the ground truth. All silicone elastomer blends were assumed to be nearly incompressible<sup>20,54</sup> and were modeled with an incompressible Neo-Hookean material model:

$$\psi = C_1(I_1 - 3) - p(J - 1). \tag{1}$$

$C_1$  is the Neo-Hookean material parameter, and  $I_1$  is the first invariant of the right Cauchy–Green deformation tensor defined as  $\mathbf{C} = \mathbf{F}^T\mathbf{F}$ . The Lagrange multiplier ( $p$ ) is

introduced to enforce incompressibility.  $J = \det(\mathbf{F})$  where  $\mathbf{F}$  is the deformation gradient tensor. For incompressible materials,  $J = 1$ . With the left Cauchy–Green deformation tensor defined as  $\mathbf{b} = \mathbf{F}\mathbf{F}^T$ , the Cauchy stress tensor reads:

$$\boldsymbol{\sigma} = \frac{2}{J} \mathbf{F} \frac{\partial \psi}{\partial \mathbf{C}} \mathbf{F}^T = 2C_1 \mathbf{b} - p. \quad (2)$$

For uniaxial extension of an incompressible material with stretch ratio  $\lambda_1 = \lambda$ , it follows that the principal stress in the stretch direction is:

$$\sigma_{11} = 2C_1 \left( \lambda^2 - \frac{1}{\lambda} \right). \quad (3)$$

The phantom material stiffness can be represented as the tangent modulus, which is the derivative of the principal Cauchy stress with respect to the stretch.

The Neo-Hookean material parameter,  $C_1$ , was estimated using nonlinear regression of the experimentally measured principal Cauchy stress vs. stretch data and used to define the ground truth material stiffness.

We calculated the coefficient of variation (standard deviation/mean  $\times 100\%$ ) in principal Cauchy stress to quantify the variation across the three samples tested for each model. We also calculated the coefficient of determination ( $R^2$ ) between the Neo-Hookean model predicted principal Cauchy stress and the experimentally determined principal Cauchy stress to quantitatively assess the fit of the material model to the experimental data.

## Imaging Experiments

We developed an MRI-compatible flow loop (Fig. 2) to simulate diastolic filling of the heart phantoms' LV, to enable acquisition of each phantom's filling kinematics using MRI, and to allow for measurement of ventricular filling pressures using pressure transducers. The phantoms were connected to the flow loop at the basal ports using custom-built, 3D printed barbed connectors designed with inlets for inserting pressure transducers (Fig. 2b). All models were fixed at the apical anchor and placed in a container filled with blood-mimicking fluid of similar MRI relaxation properties, density, and viscosity to blood (40% glycerol, 60% water, 0.75 mL/L ferumoxytol). The phantom box, which was adapted with flow ports to attach tubing was subsequently connected to an MRI-compatible, programmable flow pump (CardioFlow 5000 MR, Shelley Medical Imaging Technologies). The same blood-mimicking fluid was used to inflate the LV and fill the RV of the phantoms. A similar flow circuit was used in our lab to assess flow dynamics in synthetic aorta models using MRI.<sup>65</sup>

The flow pump was programmed to deliver square flow waveforms (peak flow rate = 300 mL/s) to inflate each heart

**Table 1** Imaging parameters for 3D SPGR and GRE Cine.

	3D SPGR	GRE Cine
TE/TR	2.17/5.5 ms	3.06/19.89 ms
FA	20°	12°
Spatial resolution	1 × 1 × 1 mm <sup>3</sup>	1 × 1 × 4 mm <sup>3</sup>
Number of slices/phases	144/NA	30/75
Matrix	220 × 320	128 × 128

phantom's LV. The phantoms' RV was fluid filled at the start of the experiment and sealed such that its volume remained constant throughout the experiment. Filling pressures were acquired in the MRI scanner room during volumetric loading, immediately prior to scanning because the pressure transducers, though MRI safe, can induce image artifacts if used during imaging and imaging can produce pressure signal artifacts.<sup>48</sup> During the inflation experiment, both intraventricular pressures were simultaneously acquired (PowerLab, LabChart 8, AD Instruments) using MRI-compatible pressure transducers (Micro-Tip SPR 350S, Millar). Pressures for ten loading cycles were acquired, with the averaged pressure cycle used as the loading pressure. The coefficient of variation in the pressure waveform across the ten measured cycles was calculated for each experiment and was used to define the uncertainty in the pressure measurements.

All *in vitro* images were collected on a 3T MRI (Skyra, Siemens) using a 32-channel spine and 18-channel body matrix coil. The reference (unloaded) geometry of the phantom was acquired using a 3D spoiled gradient echo (3D SPGR) spanning the entire volume. Cine gradient echo (GRE) images were acquired during LV inflation to capture phantom motion and to obtain filling volumes. Imaging parameters are detailed in Table 1. Ventricular filling pressures were synced with the image acquisition using a trigger.

## Data Analysis

The myocardium was semi-automatically segmented from the 3D SPGR images of the unloaded phantom. First, a morphological segmentation<sup>26,30</sup> was performed in ImageJ (v1.53q), then the final segmentation was produced after a few morphological operations and some manual cleanup. The segmentation masks were then used to generate the reference geometric models that were used for *in silico* modeling (Figs. 3a–3c).

The LV volumes during inflation were determined by semi-automatically segmenting the LV blood pool from the GRE cine images of the phantom during inflation using Otsu's method<sup>35</sup> and manual cleanup (ImageJ). For each model, the segmentation was performed on the volumetric cine short axis image stack at different phases, then the LV

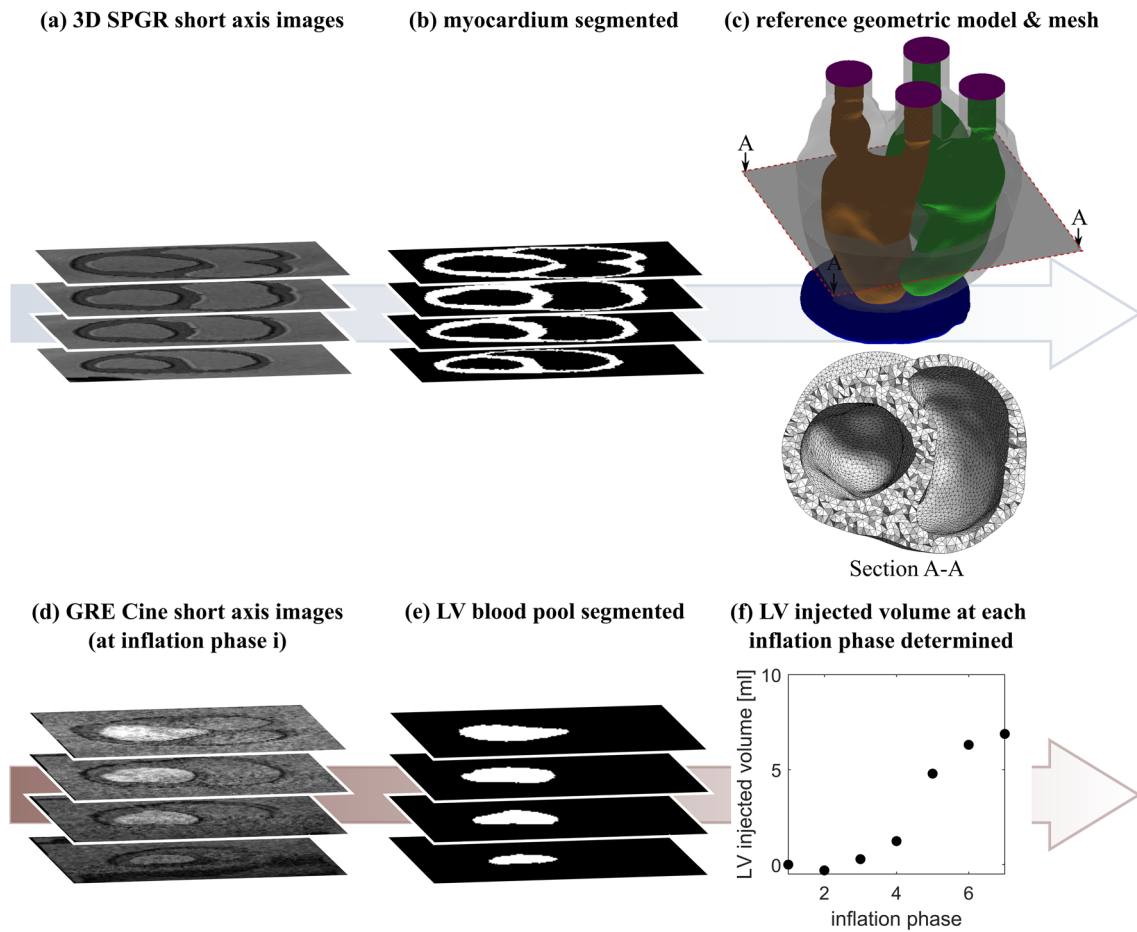


**Figure 3** (a) 3D SPGR short-axis images. (b) Myocardium segmentation is used to develop (c) the reference geometric models that are meshed with quadratic tetrahedral elements. In the finite element model, the LV endocardial surface was inflated with measured LV pressure (orange), the RV endocardial surface was inflated with measured RV pressure (green), the top surface of the basal ports were fixed

in the longitudinal direction (purple), and the apical anchor was fixed in all directions (blue). (d) GRE Cine short axis image stack at an inflation phase. (e) The LV blood pool from each inflation phase of the GRE Cine images is segmented. (f) The volume at each inflation phase is extracted from the segmentation and is used to determine the LV injected volume at each cardiac phase.

volume at each inflation phase was extracted to determine the inflation volume over time (Figs. 3d–3f).

The synced measured pressures and filling volumes were used to obtain an LV pressure–volume relationship that was used for stiffness estimation.

***In Silico* Modeling and Stiffness Quantification**

First, the geometric heart phantom models in the reference configuration (see “Data Analysis” section) were modified by virtually closing off the top surface of the ventricular basal ports. This was done to create enclosed cavities for efficient computation of the ventricular volume evolution. The 3D geometric models were meshed with standard quadratic tetrahedral elements using GMSH<sup>12</sup> (Fig. 3c). Following a mesh sensitivity study, final mesh characteristics for

**Table 2** Mesh properties.

	$M_{g1,s1}$	$M_{g1,s2}$	$M_{g1,s3}$	$M_{g2,s1}$
Number of nodes	221,714	227,874	228,105	243,540
Number of elements	134,309	138,415	138,446	150,475
Degrees of freedom	402,927	415,245	415,338	451,425
Average element volume (mm <sup>3</sup> )	1.89	1.90	1.86	1.94

each model are detailed in Table 2. The finite element model was then built to be solved using FEBio.<sup>28</sup>

Based on our tensile testing experiments (see “Ground Truth Material Characterization” section), it was shown that the silicone elastomer phantom materials can be adequately modeled using the Neo-Hookean strain energy function. Additionally, we assumed our simulated material to be nearly incompressible

following prior mechanical characterization studies on Sylgard 527 and 184.<sup>20,54</sup> We enforced incompressibility in the simulation by setting the bulk modulus to be 100 times the Neo-Hookean material parameter. Across all the models, incompressibility was well enforced, with most elements having a relative element volume at peak inflation of 1.000 and the worst elements deviating from this peak inflation volume by a maximum of 0.003. The boundary and loading conditions of the computational heart phantoms were set to match the experimental conditions. The apical anchor was kinematically constrained in all directions, while the top surfaces of the ventricular basal ports were kinematically constrained from moving in the longitudinal direction. The recorded LV and RV intraventricular pressures were measured simultaneously during the imaging experiment. During simulation, these pressures were applied to the LV and RV endocardial surfaces and the resulting phantom deformations were computed.

We set up a computational optimization scheme to deduce the phantom material stiffness from the MRI-derived LV volumes and catheter-based pressure measurements. More specifically, with FEBio as the forward solver, we used the constrained Levenberg–Marquardt optimization algorithm<sup>21</sup> (Fig. 4) to find the appropriate constitutive parameter ( $C_1$ ) that minimized the error between the simulated and experimental LV volume evolution. The material parameter optimization algorithm minimizes an objective function ( $\varphi$ ), which is the sum of the squared difference between the experimental and simulated LV volume at each inflation phase.  $C_1$  is iteratively updated to minimize  $\varphi$  until the reduction in  $\varphi$  falls below a specified tolerance ( $1e^{-3}$  kPa).

For all models, the initial guess was set as  $C_1 = 25$  kPa. We placed constraints on the possible values of  $C_1$  to ensure it remained within reasonable limits ( $1 < C_1 < 100$  kPa). Inverse parameter estimates using the upper and lower bounds of the measured pressure uncertainty were also performed to account for the uncertainty in material parameters due to pressure measurement.

The mesh size chosen for the inverse simulation was determined from a mesh convergence study and was found to lead to a variance of  $< 1\%$  LV peak inflation volume with further mesh refinement, an accuracy that was deemed appropriate for our study.

## Results

### Ground Truth Material Characterization

Principal Cauchy stress vs. stretch for representative samples of the silicone elastomer blend used to cast models  $M_{g1,s1}$ ,  $M_{g1,s2}$ ,  $M_{g1,s3}$ , and  $M_{g2,s1}$  are shown in Fig. 5. The uncertainty arises from the standard deviation of the three samples subjected to uniaxial tensile testing.

A Neo-Hookean material model was fit to the average (from three tests) stress–stretch data to obtain the ground truth material parameters. Ground truth stiffness at the peak simulated principal stretch in the *in silico* phantoms (stretch,  $\lambda = \lambda_{\text{peak}}$ ) is reported for each model (Table 3). The coefficient of variation of the experimentally determined Cauchy stress at  $\lambda_{\text{peak}}$  across the three samples was 10.4, 4.3, 2.5 and 2.8% for models  $M_{g1,s1}$ ,  $M_{g1,s2}$ ,  $M_{g1,s3}$ , and  $M_{g2,s1}$ , respectively. The  $R^2$  between the Neo-Hookean model predicted principal Cauchy stress and the experimentally determined principal Cauchy stress was over 0.99 for all models tested (Fig. 5).

### Inflation Pressure–Volume Relations

The measured LV inflation pressure and the LV inflation volumes obtained from segmenting the cine MRI images are shown in Fig. 6. The experimentally measured LV pressure vs. LV injected volume (inflation volume – initial volume) for all the models is shown in Fig. 6.

The peak LV inflation pressures were 31.6, 33.2, 78.7, and 24.1 mmHg and the peak LV injected volumes were 6.3, 5.9, 8.5, and 8.1 mL for models  $M_{g1,s1}$ ,  $M_{g1,s2}$ ,  $M_{g1,s3}$ , and  $M_{g2,s1}$ , respectively. The peak RV measured pressures were 2.1, 1.3, 1.5, and 0.9 mmHg for models  $M_{g1,s1}$ ,  $M_{g1,s2}$ ,  $M_{g1,s3}$ , and  $M_{g2,s1}$ , respectively.

### Simulated Mechanical Behavior

The computed phantom deformation and the variation in displacement magnitude at maximum inflation is shown for all four models (Fig. 7).  $\lambda_{\text{peak}}$  (Peak simulated principal stretch) in the phantoms were 1.11, 1.09, 1.13, and 1.10 for models  $M_{g1,s1}$ ,  $M_{g1,s2}$ ,  $M_{g1,s3}$ , and  $M_{g2,s1}$ , respectively.

Figure 6 (fourth row) shows that the calibrated LV pressure–volume (dotted line) corresponds well with the experimentally determined LV pressure–volume (points). Specifically, the calibrated LV pressure–volume is from a forward simulation using the optimized material parameters. The uncertain region around this simulated LV pressure–volume curve corresponds to the forward simulations using the optimized material parameters calibrated using the upper and lower uncertainty limits of the experimentally derived LV pressure–volume relationship.

The principal Cauchy stress vs. stretch from a simulated tensile test using the optimized (simulated) material parameters is shown for all models (dotted line) (Fig. 8) and compared with the ground truth mechanical behavior in uniaxial tension (solid line). From Fig. 8, we see that there is good agreement in the simulated and ground truth mechanical behavior for all models with the percent difference in Cauchy stress at  $\lambda_{\text{peak}}$  being 5.2,  $-1.0$ , 3.3, and 4.7% for models  $M_{g1,s1}$ ,  $M_{g1,s2}$ ,  $M_{g1,s3}$ , and  $M_{g2,s1}$ , respectively.

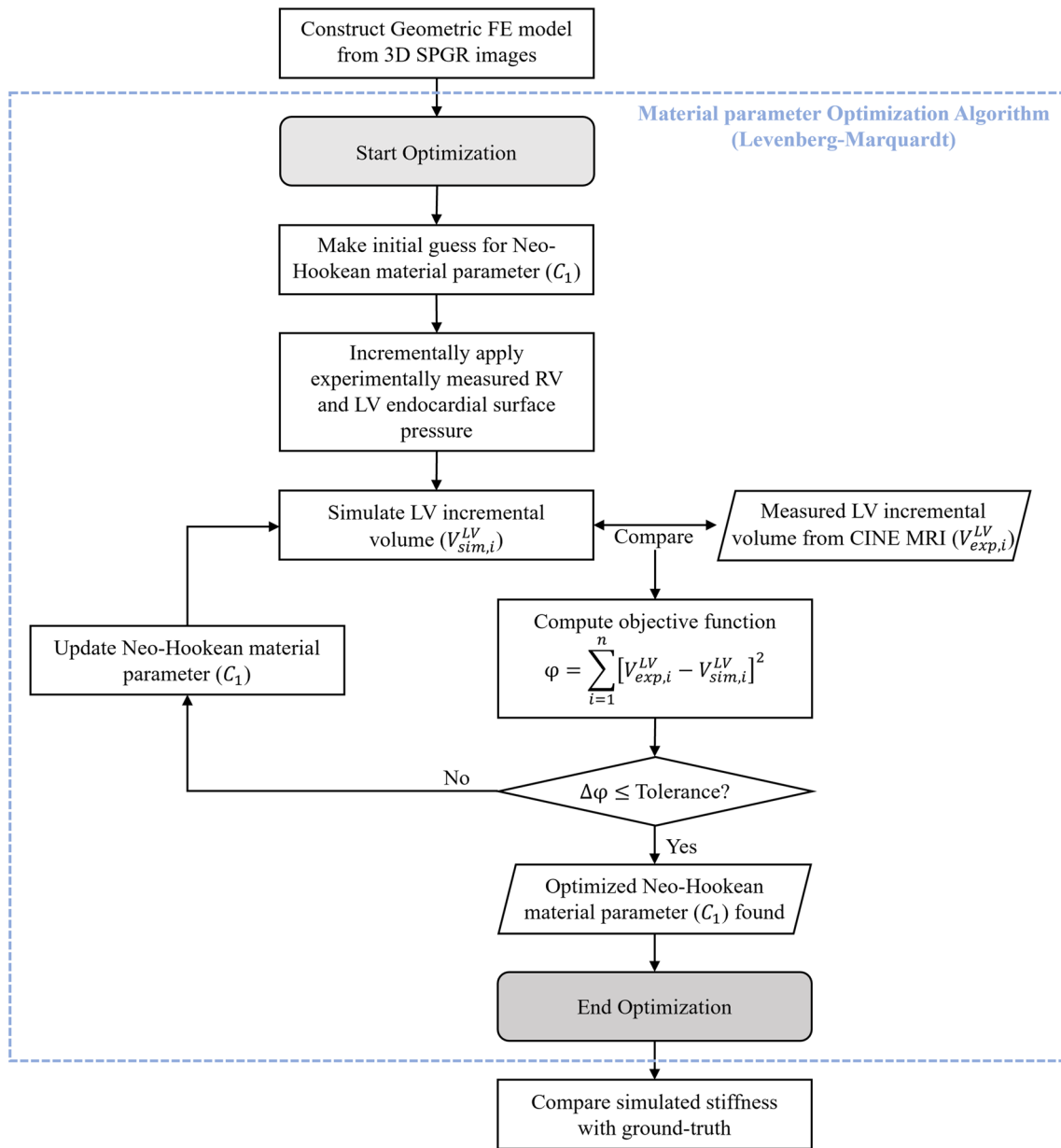


**Figure 4** Material parameter optimization flowchart. The goal is to minimize the objective function ( $\varphi$ ), which is the sum of the squared difference between the experimental LV volume ( $V_{exp}^{LV}$ ) and simulated LV volume ( $V_{sim}^{LV}$ ) at each inflation phase ( $i$ ). The parameter optimi-

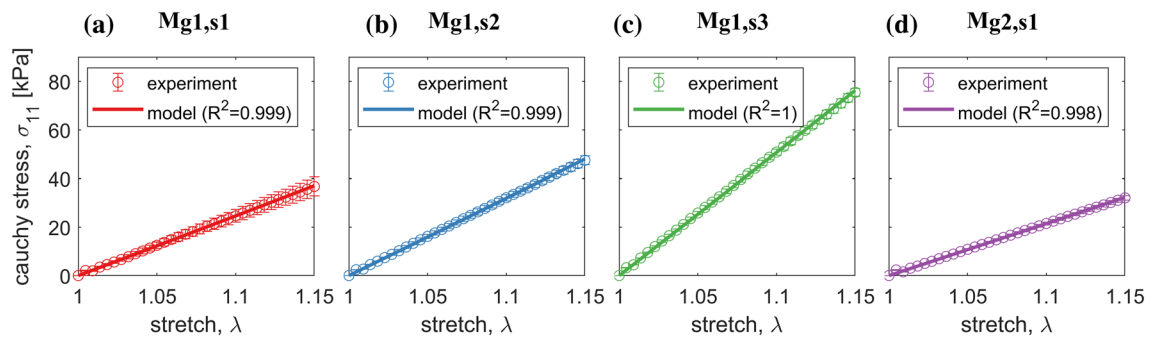
zation algorithm iteratively updates the  $C_1$  Neo-Hookean material parameter to minimize  $\varphi$  until the reduction in  $\varphi$  ( $\Delta\varphi$ ) falls below a specified tolerance which was set to  $1e^{-3}$  kPa.

Table 3 reports the ground truth and simulated stiffness (tangent modulus) at  $\lambda_{peak}$  for all models. The percentage difference between the simulated and ground truth stiffness is  $< 6\%$  for all the models.

## Discussion

### Contributions

Increased passive myocardial stiffness is a cardiac remodeling mechanism associated with a significant structural change underlying the progression of HFpEF.<sup>44,62</sup> There exist several studies leveraging cardiac MRI data and ventricular pressure measurements for the estimation of patient-specific passive myocardial stiffness. However,



**Figure 5** Cauchy stress ( $\sigma_{11}$ ) vs. stretch ( $\lambda$ ) from the ground truth uniaxial tensile tests for (a) model  $M_{g1,s1}$  (red); (b) model  $M_{g1,s2}$  (blue); (c) model  $M_{g1,s3}$  (green); and (d) model  $M_{g2,s1}$  (purple). The standard deviation arises from tests across three samples.

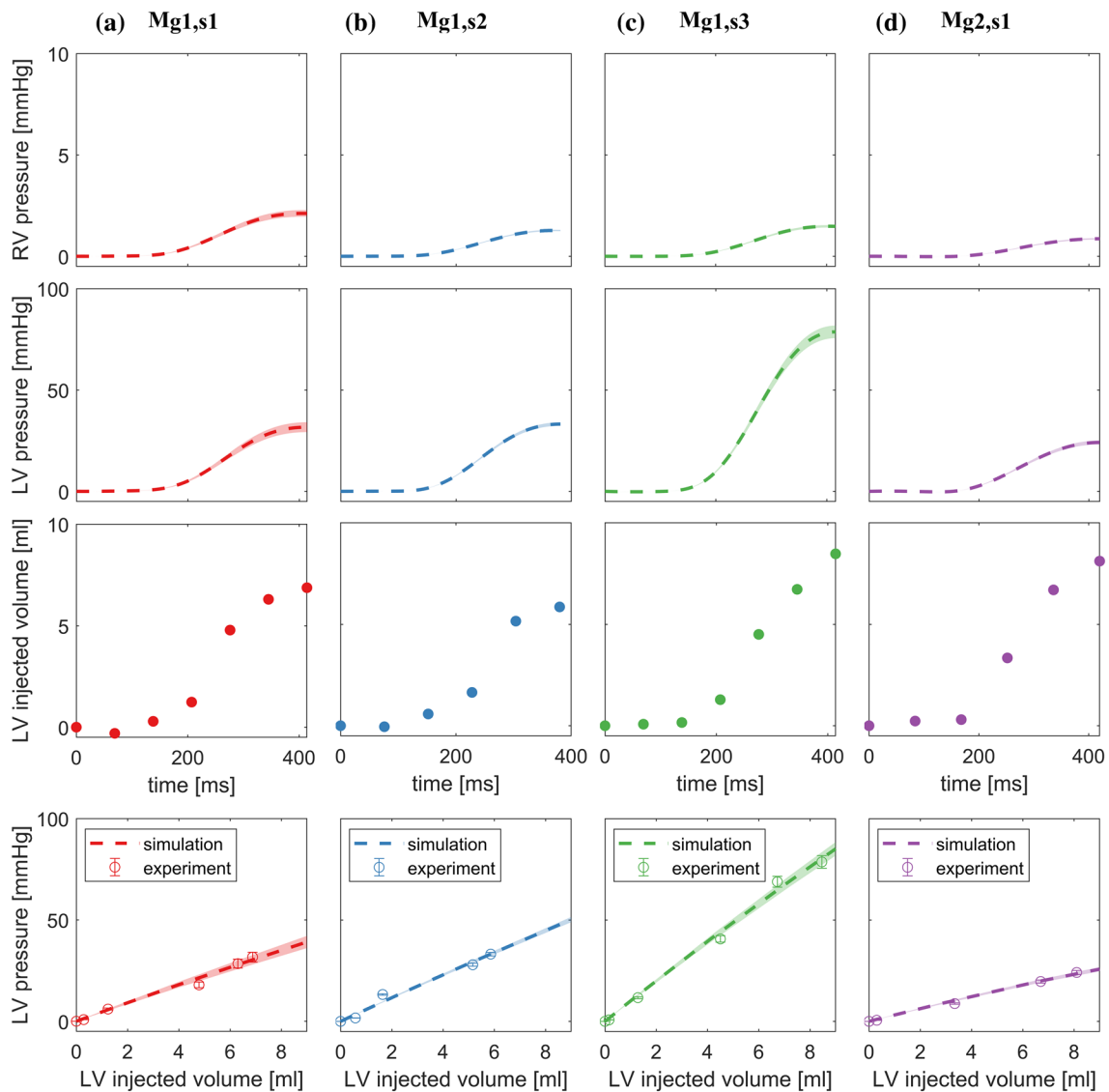


**Figure 6** Right ventricular (RV) pressure vs. time (first row), left ventricular (LV) pressure vs. time (second row), LV volume over time (third row), and experimentally measured LV pressure–volume overlaid with calibrated (optimized) LV pressure–volume (fourth row)

for (a) model  $M_{g1,s1}$  (red); (b) model  $M_{g1,s2}$  (blue); (c) model  $M_{g1,s3}$  (green); and (d) model  $M_{g2,s1}$  (purple). Uncertainty arises from the maximum coefficient of variation in measured pressures across all experiments.

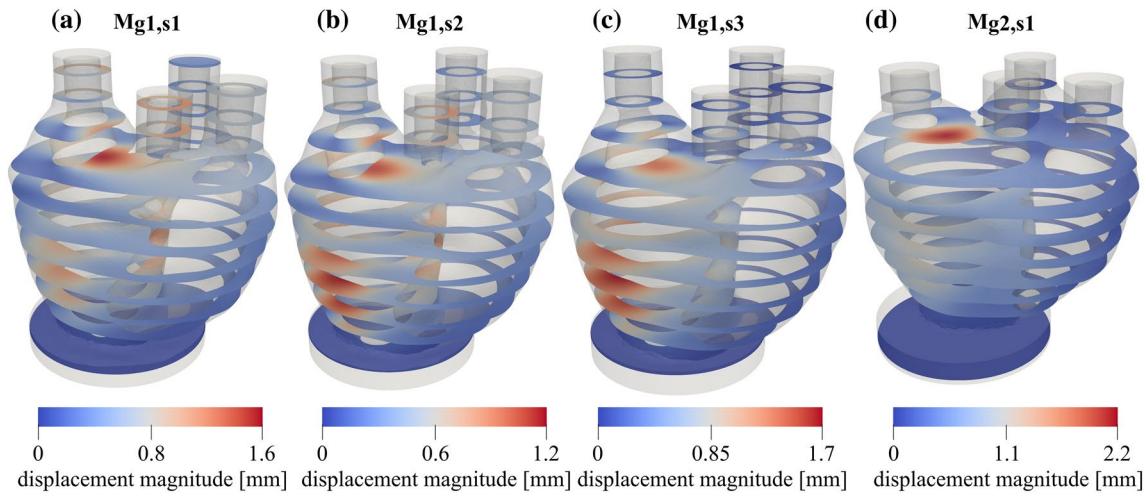


**Figure 7** Computed phantom deformation at maximum inflation. Short-axis slices show the spatial variation in displacement magnitude for (a) model  $M_{g1,s1}$ ; (b) model  $M_{g1,s2}$ ; (c) model  $M_{g1,s3}$ ; and (d) model  $M_{g2,s1}$ .

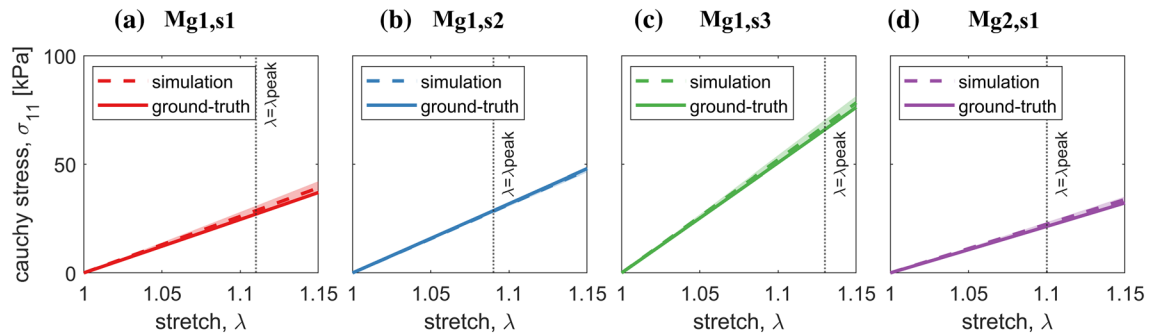


**Figure 8** Cauchy stress ( $\sigma_{11}$ ) vs. stretch ( $\lambda$ ) from uniaxial tensile tests using simulated (optimized) material parameter (dotted lines) and ground truth material parameter obtained from tensile testing (solid lines) for (a) model  $M_{g1,s1}$  (red); (b) model  $M_{g1,s2}$  (blue); (c) model

$M_{g1,s3}$  (green); and (d) model  $M_{g2,s1}$  (purple). Uncertainty arises from the maximum coefficient of variation in the measured pressures across all experiments. The peak simulated principal stretch ( $\lambda_{peak}$ ) in the models is indicated.

**Table 3** Simulated vs. ground truth mechanical behavior.

		$C_1$ (kPa)	Stiffness (kPa) ( $\lambda = \lambda_{peak}$ )	$\sigma_{11}$ (kPa) ( $\lambda = \lambda_{peak}$ )
$M_{g1,s1}$	Ground truth	$40.9 \pm 4.3$	$248.2 \pm 26.2$	$27.3 \pm 2.8$
	Simulation	$43.3 \pm 3.3$	$262.7 \pm 20.1$	$28.7 \pm 2.2$
	% Difference	5.9%	5.8%	5.2%
$M_{g1,s2}$	Ground truth	$53.0 \pm 2.1$	$320.2 \pm 12.6$	$28.6 \pm 1.2$
	Simulation	$52.4 \pm 4.0$	$316.9 \pm 24.2$	$28.4 \pm 2.2$
	% Difference	-1.0%	-1.0%	-1.0%
$M_{g1,s3}$	Ground truth	$84.2 \pm 2.1$	$512.3 \pm 12.7$	$65.6 \pm 1.7$
	Simulation	$86.5 \pm 6.6$	$526.4 \pm 40.2$	$67.8 \pm 5.2$
	% Difference	2.7%	2.7%	3.3%
$M_{g2,s1}$	Ground truth	$35.6 \pm 1.0$	$215.7 \pm 6.0$	$21.5 \pm 0.6$
	Simulation	$37.4 \pm 2.9$	$226.2 \pm 17.3$	$22.5 \pm 1.7$
	% Difference	4.9%	4.9%	4.7%

most of these studies have a common limitation—the estimated passive myocardial stiffness estimates were not comprehensively validated. This lack of validation is due, in part, to the lack of ground truth *in vivo* passive myocardial stiffness estimates available for comparison. Nevertheless, before computational models can be adopted as clinical prognostic tools, there is a need for thorough validation.

We quantitatively assessed the accuracy of MRI-driven computational modeling for myocardial stiffness estimation in four soft silicone phantoms with realistic cardiac morphometry and known ground truth mechanical behavior and stiffness. In models  $M_{g1,s1}$ ,  $M_{g1,s2}$ ,  $M_{g1,s3}$ , and  $M_{g2,s1}$ , the stiffness estimation errors were 5.8, -1.0, 2.7, and 4.9%. These low errors demonstrate the feasibility of highly accurate passive myocardial material stiffness estimation using an MRI-driven computational constitutive modeling framework. Additionally, we developed a phantom manufacturing

procedure that can reproduce phantoms of high geometric fidelity, myocardium mimicking stiffness, and heart-like MRI relaxation properties.<sup>23</sup> For all models, the estimated ground truth material stiffnesses were consistent with previous work evaluating the stiffness of Sylgard blends<sup>36</sup> (see Supplementary Fig. S1). Additionally, across all samples subjected to uniaxial tensile testing, we were able to reproduce nearly identical principal stress vs. stretch relationships and reaction force vs. displacement curves in simulated tensile tests (see Supplementary Figs. S2 and S3). We can also tune the material stiffness of the phantoms by manufacturing them with different silicone elastomer mass compositions (see “Phantom Development” section). We incorporated the heart phantoms within an MRI-compatible LV diastolic filling setup and acquired the MRI and pressure data necessary for estimating the phantoms’ LV myocardial stiffness using a finite element model. Through finite element modeling and material parameter optimization, we obtained the mechanical (Neo-Hookean) behavior and stiffness of the phantoms and compared these simulated mechanical metrics with ground truth values obtained through tensile testing.

Augenstein *et al.*<sup>4</sup> developed an experimental method for validating passive material properties of a cylindrical silicone gel phantom obtained through MRI-based computational constitutive modeling. Their simulated constitutive parameters were compared to parameters obtained independently from rotational shear testing and showed very good agreement. We extend their study by using geometrically accurate biventricular heart phantoms for validation. Additionally, we perform the validation in heart phantoms of varying stiffnesses and geometries to understand the identifiability across a range of stiffnesses independent of geometry. Our work also differs, in that Augenstein *et al.* used MRI tagging obtained displacements in their objective function, whereas we used the LV pressure–volume relationship for calibrating our computational model for material parameter optimization. Material parameter optimization using local displacements enables the construction of a richer objective function that incorporates more of the deformation kinematics, which better constrains the solution. However, MRI data for estimating local displacements (e.g., from MRI tagging or cine DENSE) is not always available in subjects or in experiments. While we used only the inflation pressure–volume relationship to calibrate the computational models, we compared the simulated end-inflation shapes with the image-obtained end-inflation shapes and found good agreement across all models (Supplementary Fig. S4).

Zhu *et al.*<sup>61</sup> used an anatomically accurate biventricular heart phantom to validate the displacements obtained from a MRI-based computational phantom. They compared displacements from a finite element forward simulation with a ground truth obtained from marker tracking using cameras. Our study extends theirs by using more physiologically

relevant loading conditions in that we applied pressures on the endocardial surface, whereas the phantom used in their study applies displacement boundary conditions on the apex to control the phantom motion. In addition, their work was focused on validating simulated displacements as opposed to material parameters or material stiffness.

### Deviations of *In Vitro* System from *In Vivo* Heart

Our phantom materials are a practical approximation of myocardium, but lack some key biomechanical features.<sup>5</sup> Notably, unlike myocardium, which is anisotropic due to the underlying microstructure, our material is isotropic. Additionally, the phantom material’s nonlinearity in the relevant stretch range differs from that which is exhibited by myocardium. Specifically, unlike myocardium which exhibits an exponential-like stress–strain relationship in uniaxial tension, our material more closely resembles a linearly elastic material in the stretch range considered.

Our phantom materials are also stiffer than healthy human ventricular myocardium. We sought to manufacture the softest heart phantom with a material of similar stiffness to healthy human myocardium. Emig *et al.*<sup>10</sup> compiled myocardial stiffness values from a range of studies and showed that the passive (diastolic) tangent stiffness of human adult hearts ranged from 8 to 70 kPa. However, caution should be taken when interpreting the stiffness values due to the wide range of estimation techniques used, myocardium constitutive laws employed, and the lack of standardization of the stretch at which the stiffnesses were estimated and reported across all studies. Nevertheless, the softest phantom we could produce demonstrated a stiffness of 215.7 kPa, which is significantly stiffer than healthy human ventricular myocardium. Our phantom manufacturing procedure can reproduce phantoms with stiffnesses closer to that of human myocardium ( $\lesssim 100$  kPa), but the far inferior workability of the softer phantoms meant our choice of material was limited to phantoms with stiffness  $\gtrsim 200$  kPa. Wang *et al.*<sup>57</sup> and Zile *et al.*<sup>63</sup> showed that in HFpEF patients, there can be myocardial stiffness increases of two to three times that of a control group. Given the range of passive myocardial stiffness of human adults (8 to 70 kPa<sup>10</sup>), model  $M_{g2,s1}$ , the softest phantom (stiffness 215.7 kPa) has comparable stiffness to the passive myocardial stiffness expected in HFpEF. The stiffest heart phantom (model  $M_{g1,s3}$ ) had a stiffness of 512.3 kPa, which is closer to the stiffness of myocardial infarcts.<sup>2</sup>

The boundary conditions of the *in vitro* phantoms were modeled appropriately in the *in silico* phantoms, but some of the applied constraints differ from those which are seen in the *in vivo* heart. For example, the basal ports were fixed longitudinally whereas *in vivo* we expect some valve plane motion. Secondly, in all the models, the apex was kinematically constrained in all directions unlike in the *in vivo* heart,

where the apex freely rotates. Additionally, as the RV volume was kept constant due to the lack of a second MRI-compatible pump to simultaneously inflate the phantom's RV, the septal mechanics are different from that which is expected *in vivo*.

Some additional complexities that exist in the *in vivo* beating heart could not be modeled by our *in vitro* system. For example, our system doesn't include pericardial interactions, which have been shown to influence myocardial mechanics.<sup>19,42</sup> Moreover, through our manufacturing procedure, we are unable to replicate the prestresses which *in vivo* myocardium is known to exhibit.<sup>34</sup> Inclusion of the influence of these myocardial prestresses which are thought to facilitate diastolic filling<sup>11</sup> and homogenize the ventricular wall stresses<sup>34</sup> can significantly impact passive myocardial stiffness estimation.<sup>11,15,33</sup> Due to these prestresses, the geometry obtained from medical images don't represent an actual unstressed reference configuration for finite element analysis even though the images may represent an externally unloaded state. Though there exist inverse methods for identifying the truly unstressed configuration,<sup>39</sup> full validation of these computational inverse prestress estimation procedures is still lacking.

Our heart phantoms do not replicate exactly, the *in vivo* heart. Nevertheless, we demonstrate our ability to use an MRI-driven computational constitutive modeling framework to identify the material parameters of soft heart-like phantoms of varying stiffness and different complex geometries. This is an important demonstration of feasibility before future *in vivo* passive myocardial stiffness estimation.

## Computational Modeling Framework

Although there are many permutations of methods to acquire and analyze the input data needed for myocardial stiffness estimation, for our study, we considered only one MRI-based framework for myocardial stiffness estimation. Other methods may introduce uncertainties not considered in this study. Additionally, we acquired relatively high-resolution imaging data which may not be feasible in clinical settings. Future work could consider the effects of downsampling the data to more clinically relevant resolutions and assessing the effects of data resolution on the stiffness estimation.

## Inflation Volumes

Our maximum inflation volumes in the phantoms were 6.3, 5.9, 8.5, and 8.1 mL for models  $M_{g1,s1}$ ,  $M_{g1,s2}$ ,  $M_{g1,s3}$ , and  $M_{g2,s1}$ , respectively. We are interested in modeling the ventricular passive filling which results from the atrial kick, responsible for 20%<sup>32</sup> of total LV filling during diastole. The normal stroke volume of healthy humans is 50 to 100 mL,<sup>47</sup> therefore to accurately model passive filling, our injection

volumes should be between 10 and 20 mL. We are only modeling a part of the diastolic filling volume differences, due to the mechanical limitations of our inflation system. However, despite this fact, we show that even at these lower kinematic differences, we can already accurately estimate the stiffness of the heart phantoms at physiological stretch conditions.

## Conclusion

We quantitatively evaluated the accuracy of MRI-driven computational modeling to estimate myocardial stiffness using personalized soft heart phantoms of varying stiffness and geometry. Our study obtained excellent agreement with an independently obtained ground truth stiffness and demonstrates the utility of MRI-driven constitutive modeling to estimate myocardial stiffness in the beating heart, non-invasively and *in vivo*.

**Supplementary Information** The online version of this article (doi:<https://doi.org/10.1007/s10439-023-03164-7>) contains supplementary material, which is available to authorized users.

**Acknowledgments** F.K. receives research support from the Stanford Bio-X Stanford Interdisciplinary Graduate Fellowship. This project was funded, in part, by NIH R01 HL131823 to D.B.E.

**Conflict of interest** No benefits in any form have been or will be received from a commercial party related directly or indirectly to the subject of this manuscript.

## References

1. Aliotta, E., K. Moulin, P. Magrath, and D. B. Ennis. Quantifying precision in cardiac diffusion tensor imaging with second-order motion-compensated convex optimized diffusion encoding. *Magn. Reson. Med.* 80:1074–1087, 2018.
2. Arunachalam, S. P., A. Arani, F. Baffour, J. A. Rysavy, P. J. Rossman, K. J. Glaser, D. S. Lake, J. D. Trzasko, A. Manduca, K. P. McGee, R. L. Ehman, and P. A. Araoz. Regional assessment of *in vivo* myocardial stiffness using 3D magnetic resonance elastography in a porcine model of myocardial infarction. *Magn. Reson. Med.* 79:361–369, 2018.
3. Asner, L., M. Hadjicharalambous, R. Chabiniok, D. Peresutti, E. Sammut, J. Wong, G. Carr-White, P. Chowienczyk, J. Lee, A. King, N. Smith, R. Razavi, and D. Nordsletten. Estimation of passive and active properties in the human heart using 3D tagged MRI. *Biomech. Model. Mechanobiol.* 15:1121–1139, 2016.
4. Augenstein, K. F., B. R. Cowan, I. J. LeGrice, P. M. F. Nielsen, and A. A. Young. Method and apparatus for soft tissue material parameter estimation using tissue tagged Magnetic Resonance Imaging. *J. Biomech. Eng.* 127:148–157, 2005.
5. Avazmohammadi, R., J. S. Soares, D. S. Li, S. S. Raut, R. C. Gorman, and M. S. Sacks. A contemporary look at biomechanical models of myocardium. *Annu. Rev. Biomed. Eng.* 21:417–442, 2019.
6. Channer, K. S., W. Culling, P. Wilde, and J. V. Jones. Estimation of left ventricular end-diastolic pressure by pulsed Doppler ultrasound. *Lancet* 1:1005–1007, 1986.

7. Cork, T. E., L. E. Perotti, I. A. Verzhbinsky, M. Loecher, and D. B. Ennis. High-resolution ex vivo microstructural MRI after restoring ventricular geometry via 3D printing. *Funct. Imaging Model. Heart* 11504:177–186, 2019.
8. Coronel, R., J. de Groot, and J. van Lieshout. Defining heart failure. *Cardiovasc. Res.* 50:419–422, 2001.
9. Dual, S. A., J. M. Zimmermann, J. Neuenschwander, N. H. Cohrs, N. Solowjowa, W. J. Stark, M. Meboldt, and M. SchmidDaners. Ultrasonic sensor concept to fit a ventricular assist device cannula evaluated using geometrically accurate heart phantoms. *Artif. Organs* 43:467–477, 2019.
10. Emig, R., C. M. Zgierski-Johnston, V. Timmermann, A. J. Taberner, M. P. Nash, P. Kohl, and R. Peyronnet. Passive myocardial mechanical properties: meaning, measurement, models. *Biophys. Rev.* 13:587–610, 2021.
11. Genet, M., M. Rausch, L. Lee, S. Choy, X. Zhao, G. Kassab, S. Kozerke, J. Guccione, and E. Kuhl. Heterogeneous growth-induced prestrain in the heart. *J. Biomech.* 48:2080–2089, 2015.
12. Geuzaine, C., and J.-F. Remacle. GMSH: a 3-D finite element mesh generator with built-in pre- and post-processing facilities. *Int. J. Numer. Methods Eng.* 79:1309–1331, 2009.
13. Greenberg, N. L., P. M. Vandervoort, M. S. Firstenberg, M. J. Garcia, and J. D. Thomas. Estimation of diastolic intraventricular pressure gradients by Doppler M-mode echocardiography. *Am. J. Physiol. Heart Circ. Physiol.* 280:H2507–2515, 2001.
14. Guccione, J. M., K. D. Costa, and A. D. McCulloch. Finite element stress analysis of left ventricular mechanics in the beating dog heart. *J. Biomech.* 28:1167–1177, 1995.
15. Hadjicharalambous, M., C. T. Stoeck, M. Weisskopf, N. Cesarovic, E. Ioannou, V. Vavourakis, and D. A. Nordsletten. Investigating the reference domain influence in personalised models of cardiac mechanics: effect of unloaded geometry on cardiac biomechanics. *Biomech. Model. Mechanobiol.* 20:1579–1597, 2021.
16. Henning, R. J. Diagnosis and treatment of heart failure with preserved left ventricular ejection fraction. *World J. Cardiol.* 12:7–25, 2020.
17. Hopf, R., L. Bernardi, J. Menze, M. Zündel, E. Mazza, and A. E. Ehret. Experimental and theoretical analyses of the age-dependent large-strain behavior of Sylgard 184 (10:1) silicone elastomer. *J. Mech. Behav. Biomed. Mater.* 60:425–437, 2016.
18. Hunter, P. J., A. J. Pullan, and B. H. Smaill. Modeling total heart function. *Annu. Rev. Biomed. Eng.* 5:147–177, 2003.
19. Jöbssis, P. D., H. Ashikaga, H. Wen, E. C. Rothstein, K. A. Horvath, E. R. McVeigh, and R. S. Balaban. The visceral pericardium: macromolecular structure and contribution to passive mechanical properties of the left ventricle. *Am. J. Physiol. Heart Circ. Physiol.* 293:H3379–3387, 2007.
20. Johnston, I. D., D. K. McCluskey, C. K. L. Tan, and M. C. Tracey. Mechanical characterization of bulk Sylgard 184 for microfluidics and microengineering. *J. Micromech. Microeng.* 24:035017, 2014.
21. Kanzow, C., N. Yamashita, and M. Fukushima. Levenberg–Marquardt methods with strong local convergence properties for solving nonlinear equations with convex constraints. *J. Comput. Appl. Math.* 172:375–397, 2004.
22. Kass, D. A., J. G. F. Bronzwaer, and W. J. Paulus. What mechanisms underlie diastolic dysfunction in heart failure? *Circ. Res.* 94:1533–1542, 2004.
23. Kolawole, F. O., M. Peirlinck, T. E. Cork, V. Y. Wang, S. A. Dual, M. E. Levenston, E. Kuhl, and D. B. Ennis. A framework for evaluating myocardial stiffness using 3D-printed heart phantoms. In: *Functional Imaging and Modeling of the Heart*, edited by D. B. Ennis, L. E. Perotti, and V. Y. Wang. Cham: Springer, 2021, pp. 305–314.
24. Krishnamurthy, A., C. T. Villongco, J. Chuang, L. R. Frank, V. Nigam, E. Belezouli, P. Stark, D. E. Krummen, S. Narayan, J. H. Omens, A. D. McCulloch, and R. C. Kerckhoffs. Patient-specific models of cardiac biomechanics. *J. Comput. Phys.* 244:4–21, 2013.
25. Land, S., V. Gurev, S. Arens, C. M. Augustin, L. Baron, R. Blake, C. Bradley, S. Castro, A. Crozier, M. Favino, T. E. Fastl, T. Fritz, H. Gao, A. Gizzi, B. E. Griffith, D. E. Hurtado, R. Krause, X. Luo, M. P. Nash, S. Pezzuto, G. Plank, S. Rossi, D. Ruprecht, G. Seemann, N. P. Smith, J. Sundnes, J. J. Rice, N. Trayanova, D. Wang, Z. JennyWang, and S. A. Niederer. Verification of cardiac mechanics software: benchmark problems and solutions for testing active and passive material behaviour. *Proc. Math. Phys. Eng. Sci.* 471:20150641, 2015.
26. Legland, D., I. Arganda-Carreras, and P. Andrey. MorphoLibJ: integrated library and plugins for mathematical morphology with ImageJ. *Bioinformatics* 32:3532–3534, 2016.
27. Lippi, G., and F. Sanchis-Gomar. Global epidemiology and future trends of heart failure. *AME Med. J.* 5:15, 2020.
28. Maas, S. A., B. J. Ellis, G. A. Ateshian, and J. A. Weiss. FEBio: finite elements for biomechanics. *J. Biomech. Eng.* 134:11005, 2012.
29. Maggioni, A. P., U. Dahlström, G. Filippatos, O. Chioncel, M. Crespo Leiro, J. Drozd, F. Fruhwald, L. Gullestad, D. Logeart, G. Fabbri, R. Urso, M. Metra, J. Parissis, H. Persson, P. Ponikowski, M. Rauchhaus, A. A. Voors, O. W. Nielsen, F. Zannad, L. Tavazzi, and Heart Failure Association of the European Society of Cardiology (HFA). EURObservational research programme: regional differences and 1-year follow-up results of the heart failure pilot survey (ESC-HF pilot). *Eur. J. Heart. Fail.* 15:808–817, 2013.
30. Meyer, F., and S. Beucher. Morphological segmentation. *J. Vis. Commun. Image Represent.* 1:21–46, 1990.
31. Mojsenjenko, D., J. R. McGarvey, S. M. Dorsey, J. H. Gorman, J. A. Burdick, J. J. Pilla, R. C. Gorman, and J. F. Wenk. Estimating passive mechanical properties in a myocardial infarction using MRI and finite element simulations. *Biomech. Model. Mechanobiol.* 14:633–647, 2015.
32. Namana, V., S. S. Gupta, N. Sabharwal, and G. Hollander. Clinical significance of atrial kick. *QJM* 111:569–570, 2018.
33. Nikou, A., S. M. Dorsey, J. R. McGarvey, J. H. Gorman, J. A. Burdick, J. J. Pilla, R. C. Gorman, and J. F. Wenk. Effects of using the unloaded configuration in predicting the in vivo diastolic properties of the heart. *Comput. Methods Biomech. Biomed. Eng.* 19:1714–1720, 2016.
34. Omens, J. H., and Y. C. Fung. Residual strain in rat left ventricle. *Circ. Res.* 66:37–45, 1990.
35. Otsu, N. A threshold selection method from gray-level histograms. *IEEE Trans. Syst. Man Cybern. Syst.* 9:62–66, 1979.
36. Palchesko, R. N., L. Zhang, Y. Sun, and A. W. Feinberg. Development of polydimethylsiloxane substrates with tunable elastic modulus to study cell mechanobiology in muscle and nerve. *PLoS ONE* 7:e51499, 2012.
37. Palit, A., S. K. Bhudia, T. N. Arvanitis, G. A. Turley, and M. A. Williams. In vivo estimation of passive biomechanical properties of human myocardium. *Med. Biol. Eng. Comput.* 56:1615–1631, 2018.
38. Peirlinck, M., F. S. Costabal, J. Yao, J. M. Guccione, S. Tripathy, Y. Wang, D. Ozturk, P. Segars, T. M. Morrison, S. Levine, and E. Kuhl. Precision medicine in human heart modeling: perspectives, challenges, and opportunities. *Biomech. Model. Mechanobiol.* 20:803–831, 2021.
39. Peirlinck, M., M. De Beule, P. Segers, and N. Rebelo. A modular inverse elastostatics approach to resolve the pressure-induced stress state for in vivo imaging based cardiovascular modeling. *J. Mech. Behav. Biomed. Mater.* 85:124–133, 2018.
40. Peirlinck, M., F. SahliCostabal, K. L. Sack, J. S. Choy, G. S. Kassab, J. M. Guccione, M. De Beule, P. Segers, and E. Kuhl. Using machine learning to characterize heart failure across the scales. *Biomech. Model. Mechanobiol.* 18:1987–2001, 2019.

41. Peirlinck, M., K. L. Sack, P. De Backer, P. Morais, P. Segers, T. Franz, and M. De Beule. Kinematic boundary conditions substantially impact in silico ventricular function. *Int. J. Numer. Methods Biomed. Eng.* 35:e3151, 2019.
42. Pfaller, M. R., J. M. Hörmann, M. Weigl, A. Nagler, R. Chabiniok, C. Bertoglio, and W. A. Wall. The importance of the pericardium for cardiac biomechanics: from physiology to computational modeling. *Biomech. Model. Mechanobiol.* 18:503–529, 2019.
43. Rodríguez-Cantano, R., J. Sundnes, and M. E. Rognes. Uncertainty in cardiac myofiber orientation and stiffnesses dominate the variability of left ventricle deformation response. *Int. J. Numer. Methods Biomed. Eng.* 35:e3178, 2019.
44. Røe, Å. T., J. M. Aronsen, K. Skårdal, N. Hamdani, W. A. Linke, H. E. Danielsen, O. M. Sejersted, I. Sjaastad, and W. E. Louch. Increased passive stiffness promotes diastolic dysfunction despite improved  $Ca^{2+}$  handling during left ventricular concentric hypertrophy. *Cardiovasc. Res.* 113:1161–1172, 2017.
45. Sakata, Y., T. Ohtani, Y. Takeda, K. Yamamoto, and T. Mano. Left ventricular stiffening as therapeutic target for heart failure with preserved ejection fraction. *Circ. J.* 77:886–892, 2013.
46. Savarese, G., and L. H. Lund. Global public health burden of heart failure. *Card. Fail. Rev.* 3:7–11, 2017.
47. Sidebotham, D., and I. J. Le Grice. Chapter 1—physiology and pathophysiology. In: *Cardiothoracic Critical Care*, edited by D. Sidebotham, A. Mckee, M. Gillham, and J. H. Levy, Philadelphia: Butterworth-Heinemann, 2007, pp. 3–27.
48. Stehlin, E. F., D. McCormick, S. C. Malpas, B. P. Pontré, P. A. Heppner, and D. M. Budgett. MRI interactions of a fully implantable pressure monitoring device. *J. Magn. Reson. Imaging* 42:1441–1449, 2015.
49. Stimm, J., D. A. Nordsletten, J. Jilberto, R. Miller, E. Berberoğlu, S. Kozerke, and C. T. Stoeck. Personalization of biomechanical simulations of the left ventricle by in vivo cardiac DTI data: impact of fiber interpolation methods. *Front. Physiol.* 13:1042537, 2022.
50. Suinesiaputra, A., B. R. Cowan, A. O. Al-Agamy, M. A. Elattar, N. Ayache, A. S. Fahmy, A. M. Khalifa, P. Medrano-Gracia, M.-P. Jolly, A. H. Kadish, D. C. Lee, J. Margeta, S. K. Warfield, and A. A. Young. A collaborative resource to build consensus for automated left ventricular segmentation of cardiac MR images. *Med. Image Anal.* 18:50–62, 2014.
51. Trankle, C., J. M. Canada, L. Buckley, S. Carbone, D. Dixon, R. Arena, B. Van Tassell, and A. Abbate. Impaired myocardial relaxation with exercise determines peak aerobic exercise capacity in heart failure with preserved ejection fraction. *ESC Heart Fail.* 4:351–355, 2017.
52. Virani, S. S., A. Alonso, H. J. Aparicio, E. J. Benjamin, M. S. Bittencourt, C. W. Callaway, A. P. Carson, A. M. Chamberlain, S. Cheng, F. N. Delling, M. S. V. Elkind, K. R. Evenson, J. F. Ferguson, D. K. Gupta, S. S. Khan, B. M. Kissela, K. L. Knutson, C. D. Lee, T. T. Lewis, J. Liu, M. S. Loop, P. L. Lutsey, J. Ma, J. Mackey, S. S. Martin, D. B. Matchar, M. E. Mussolino, S. D. Navaneethan, A. M. Perak, G. A. Roth, Z. Samad, G. M. Satou, E. B. Schroeder, S. H. Shah, C. M. Shay, A. Stokes, L. B. VanWagner, N.-Y. Wang, C. W. Tsao, and American Heart Association Council on Epidemiology and Prevention Statistics Committee and Stroke Statistics Subcommittee. Heart disease and stroke statistics—2021 update: a report from the American Heart Association. *Circulation* 143:e254–e743, 2021.
53. Walker, J. C., M. B. Ratcliffe, P. Zhang, A. W. Wallace, E. W. Hsu, D. A. Saloner, and J. M. Guccione. Magnetic resonance imaging-based finite element stress analysis after linear repair of left ventricular aneurysm. *J. Thorac. Cardiovasc. Surg.* 135:1094–1102, 1102.e1–2, 2008.
54. Wang, B., and S. Krause. Properties of dimethylsiloxane microphases in phase-separated dimethylsiloxane block copolymers. *Macromolecules* 20:2201–2208, 1987.
55. Wang, V. Y., H. I. Lam, D. B. Ennis, B. R. Cowan, A. A. Young, and M. P. Nash. Modelling passive diastolic mechanics with quantitative MRI of cardiac structure and function. *Med. Image Anal.* 13:773–784, 2009.
56. Wang, V. Y., P. M. F. Nielsen, and M. P. Nash. Image-based predictive modeling of heart mechanics. *Annu. Rev. Biomed. Eng.* 17:351–383, 2015.
57. Wang, Z. J., V. Y. Wang, C. P. Bradley, M. P. Nash, A. A. Young, and J. J. Cao. Left ventricular diastolic myocardial stiffness and end-diastolic myofibre stress in human heart failure using personalised biomechanical analysis. *J. Cardiovasc. Transl. Res.* 11:346–356, 2018.
58. Watanabe, S., J. Shite, H. Takaoka, T. Shinke, Y. Tanino, H. Otake, D. Matsumoto, D. Ogasawara, T. Sawada, K.-I. Hirata, and M. Yokoyama. Predictive importance of left ventricular myocardial stiffness for the prognosis of patients with congestive heart failure. *J. Cardiol.* 58:245–252, 2011.
59. Xi, J., P. Lamata, S. Niederer, S. Land, W. Shi, X. Zhuang, S. Ourselein, S. G. Duckett, A. K. Shetty, C. A. Rinaldi, D. Rueckert, R. Razavi, and N. P. Smith. The estimation of patient-specific cardiac diastolic functions from clinical measurements. *Med. Image Anal.* 17:133–146, 2013.
60. Zhang, W., D. S. Li, T. Bui-Thanh, and M. S. Sacks. Simulation of the 3D hyperelastic behavior of ventricular myocardium using a finite-element based neural-network approach. *Comput. Methods. Appl. Mech. Eng.* 394:114871, 2022.
61. Zhu, Y., X. Luo, H. Gao, C. McComb, and C. Berry. A numerical study of a heart phantom model. *Int. J. Comput. Math.* 91:1535–1551, 2014.
62. Zile, M. R., C. F. Baicu, and W. H. Gaasch. Diastolic heart failure—abnormalities in active relaxation and passive stiffness of the left ventricle. *N. Engl. J. Med.* 350:1953–1959, 2004.
63. Zile, M. R., C. F. Baicu, J. S. Ikonomidis, R. E. Stroud, P. J. Nietert, A. D. Bradshaw, R. Slater, B. M. Palmer, P. Van Buren, M. Meyer, M. M. Redfield, D. A. Bull, H. L. Granzier, and M. M. LeWinter. Myocardial stiffness in patients with heart failure and a preserved ejection fraction: contributions of collagen and titin. *Circulation* 131:1247–1259, 2015.
64. Zile, M. R., W. H. Gaasch, J. D. Carroll, M. D. Feldman, G. P. Aurigemma, G. L. Schaer, J. K. Ghali, and P. R. Liebson. Heart failure with a normal ejection fraction. *Circulation* 104:779–782, 2001.
65. Zimmermann, J., M. Loecher, F. O. Kolawole, K. Bäumlner, K. Gifford, S. A. Dual, M. Levenston, A. L. Marsden, and D. B. Ennis. On the impact of vessel wall stiffness on quantitative flow dynamics in a synthetic model of the thoracic aorta. *Sci. Rep.* 11:6703, 2021.

**Publisher's Note** Springer Nature remains neutral with regard to jurisdictional claims in published maps and institutional affiliations.

Springer Nature or its licensor (e.g. a society or other partner) holds exclusive rights to this article under a publishing agreement with the author(s) or other rightsholder(s); author self-archiving of the accepted manuscript version of this article is solely governed by the terms of such publishing agreement and applicable law.